
# Initial development of pencil-beam scatterometer coastal processing

## OSI_VS20_01

Authors: **G. Grieco**[1], M. Portabella[1], J. Vogelzang[2], A. Verhoef[2], A. Stoffelen[2]

[1] Barcelona Expert Center (BEC ICM-CSIC)

[2] Koninklijk Nederlands Meteorologisch Instituut (KNMI)

Visiting Scientisc Activity

Technical Report

Date: 31 October 2020

# Contents



# Abstract

Accurate high-resolution QuikSCAT-derived winds with dense coastal sampling are strategic for both scientific and civil applications. The implementation of the QuikSCAT Spatial Response Function (SRF) analytical model and its parameterized version by means of a pre-computed look-up-table (LUT) provided by the Brigham Young University are described. The procedure for the computation of the Land Contribution Ratio (LCR) index has been also implemented. An optimized use of a high-spatial-resolution Land-Sea Mask (LSM) is described. Finally, an LCR-based procedure for the correction of the backscattered normalized radar cross section ($\sigma_0$) has been implemented. Both analytical and LUT-derived SRF versions have been visually validated, together with the derived LCR indexes. The distribution of the coastal $\sigma_0$s corresponding to a coastal test area of the Gulf of Taranto, in the south of Italy has been discussed. The main outcomes of this study show that the thorough characterization and exploitation of the full resolution $\sigma_0$ noise properties is fundamental for the success of the wind field retrieval close to the coast. Finally, future developments of the coastal processor are proposed. Most of these developments will be carried-out in the context of a recently approved EUMETSAT Visiting Science Activity (VSA).

# 1 Introduction

Coastal winds affect marine activities, wave and surge conditions, port safety and so forth, they also determine the local micro-climate and play a leading role in advection and dispersion of pollutants both in atmosphere and in ocean, as they affect coastal currents. Therefore, accurate coastal winds are of paramount importance for both civil and scientific applications. Recent studies demonstrate that the characterization of size and orientation of the Spatial Response Function (SRF) of scatterometer measurements is fundamental for improving both the accuracy and the sampling of coastal winds. The Land Contribution Ratio (LCR) was first proposed by [1] for improving the accuracy and the coastal sampling of SeaWinds-derived winds.
A method was developed to quantify the land contribution of each measurement. The LCR is defined as the ratio of the footprint area contaminated by land and the total footprint area. The LCR has been used to select the most favourable slice orientation (parallel to the coast) and discard the most contaminated ones. This way, the coastal sampling improves. Also the accuracy of the retrieved wind field takes advantage of this filtering, becoming comparable to that of the open ocean. This methodology was later proposed in the context of ASCAT by [2], where a parameterization of the SRF is also proposed, in order to speed-up the computation of the LCR. High-resolution ASCAT-derived winds were validated in [3]. Recently, [4] show a more comprehensive way of exploiting the LCR index. Indeed, it is used both for filtering out the footprints with high land contribution and for correcting the $\sigma_0$s that are slightly contaminated.
Even if the LCR methodology has been largely documented, the derived QuikSCAT coastal products are not yet available. Therefore, the OSI SAF aims at retrieving a coastal product from QuikSCAT acquisitions spanning its entire lifetime, by taking advantage of the LCR methodology. Moreover, the methodology will be implemented in publicly available software for pencil-beam scatterometer wind processing (PenWP) [5]. This document reports on the estimation of the SRF and the computation of the derived LCR, as described in [1].
Section 2 provides some basics about the design of SeaWinds, the model of the SRF, the LCR definition and the LCR-based $\sigma_0$ correction methodology. Section 3 shows how the SRF model and the LCR computation have been implemented. Section 4 shows the results of their implementation and validation on a test area. Furthermore, some examples relating to the distribution of $\sigma_0$ in coastal areas will be shown. Section 5 details the conclusions of this study, while section 6 lists the proposed developments of future works.

# 2 Background

A pencil-beam scatterometer uses of a dish antenna rotating with a constant angular velocity. It emits electromagnetic pulses with a carrier frequency in the microwaves and collects the back-scattered echo. Figure 1 represents an illustration of the SeaWinds scatterometer, which flew onboard the NASA polar orbiting satellite mission QuikSCAT from June 1999 until 2009. The basic features of this schema are common also to other pencil-beam satellite scatterometers, such as the Chinese HY-2 series and the Indian Oceansat-2 and SCATSAT-1.
The content of this report is entirely focused on the measurements of the QuikSCAT mission, therefore, some additional details are given about SeaWinds. For further additional details, please refer to [6] and references therein. SeaWinds is a Ku-band scatterometer, with a carrier frequency of 13.4 Ghz. It has a 1-m diameter dish antenna rotating at a rate of 18 revolutions per minute (rpm). SeaWinds generates two pencil beams: an "inner" one, with horizontal polarization and elevation angle of $40^o$, and an "outer" one, with vertical polarization and elevation angle of $46^o$. Each point on the Earth surface within 700 km from the satellite sub-track is viewed two times by the inner beam and two times by the outer one. The points lying between 700 and 900 km from the satellite sub-track are viewed (twice) only by the outer beam. SeaWinds pulses are modulated in frequency with a linear chirp. This improves the range resolution.
The SeaWinds 3 dB footprint of the inner (outer) beam has the shape of an ellipse, better known as egg, whose linear dimensions are approximately 24 (26) km and 31 (36) km respectively in azimuth and range. Thanks to the range-filtering, each egg is resolved in 10 slices, the central 8 of which are available in the full resolution (FR) files. These files are freely downloadable from the PODAAC website (https://opendap.jpl.nasa.gov/opendap/).

The LCR is defined as the ratio of the footprint area contaminated by land and the total footprint area, as follows:

$$LCR = \frac{\sum_{xy} L_{xy} S_{xy}}{\sum_{xy} S_{xy}} \tag{2.1}$$

where $L_{xy}$ is a binary Land-Sea Mask (LSM) and $S_{xy}$ is the SRF. $L_{xy}$ may be equal to 0 (sea) or 1 (land). The software for the computation of the SRF is not available from JPL NASA, but a look-up-table (LUT) of parameterized SRFs has been kindly provided by Prof. Dave Long of the Brigham Young University. According to this parameterization, the SRF is a function of the antenna azimuth angle, the orbit time, the beam identifier (inner or outer),

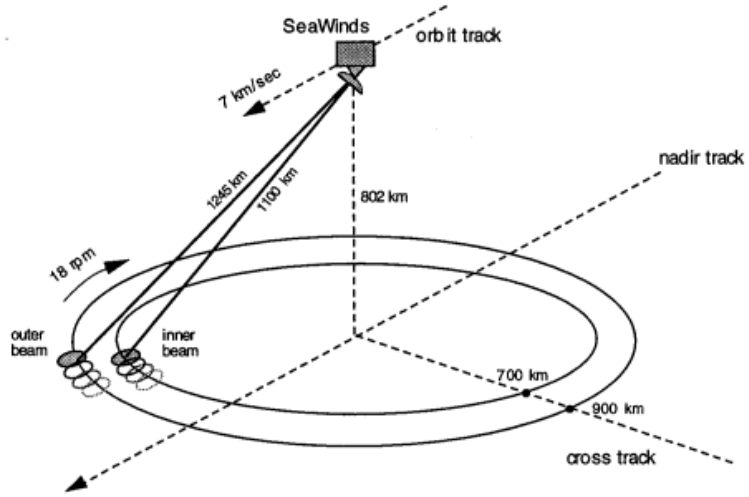


Figure 1: SeaWinds design [6]

the egg centroid latitude and the node index. The computation of the LUT derived SRFs is a two step process. First, the LUT is queried with the proper input parameters. Then, the slice SRF is centered around the slice centroid. This step is necessary because SRFs maybe rather mis-placed with respect to the slice centroid, which is empirically determined. The relocation procedure is described as follows:

$$\lambda_i^C = \lambda_i - \bar{\lambda} + \lambda^{sl} \tag{2.2}$$

$$\phi_i^C = \phi_i - \bar{\phi} + \phi^{sl} \tag{2.3}$$

$$\bar{\lambda} = \frac{1}{N}\sum_{i=1}^{N}\lambda_i \tag{2.4}$$

$$\bar{\phi} = \frac{1}{N}\sum_{i=1}^{N}\phi_i \tag{2.5}$$

with $\lambda_i$ and $\phi_i$ being the longitude and the latitude of the i$th$ point of the SRF, $\lambda_i^C$ and $\phi_i^C$ their corrected values respectively. $N$ the total number of points of the SRF, and $\bar{\lambda}$ and $\bar{\phi}$ the average longitude and latitude before the correction and $\lambda^{sl}$ and $\phi^{sl}$ the longitude and latitude of the slice centroid, respectively. However, we infer a definition where SRFs are not exactly centered around the slice centroid. This aspect is better clarified in section 4.
$S$ can be computed following the formula depicted in [1], which is here re-

ported for the sake of completeness:

$$S(\bar{l}_i) = \frac{C^2 g_i(t_{trs}) g_i(t_{rec})}{T_p r_i^4} \sum_{k=k_s}^{k_e} \left[ \frac{sin^2 \left[ \pi N_{p,i} \left( f_{b,i} T - \frac{k}{N} \right) \right]}{sin^2 \left[ \pi \left( f_{b,i} T - \frac{k}{N} \right) \right]} \right] \tag{2.6}$$

$C^2$ is defined as follows

$$C^2 = \left( \frac{\lambda^2}{(4\pi)^3} \right) \left( \frac{E_t G_r G_p^2}{L_{sys}} \right) \tag{2.7}$$

where $\lambda$ is the carrier wavelength, $E_t$ is the total energy in the transmit pulse, $G_r$ is the receiver gain, $G_p^2$ is the peak antenna gain and $L_{sys}$ is the two-way path loss. $E_t$ is set to 110 W, $G_r$ to 1, $G_p$ to 38.5 and 39 dB respectively for H-pol and V-pol pulses, and $L_{sys}$ to 1.
Note that the constant parameters fall out of equation 2.1 and are not relevant.
$g_i$ is the transmitter/receiver antenna gain pattern. The arguments $t_{trs}$ and $t_{rec}$ stand for the transmitting and receiving times respectively. They stress the fact that the antenna is rotating while emitting and receiving the pulses. $r_i$ is the range distance to the target point on the surface, $T_p$ is the integration time, $T$ is the sampling period and $k$ represents the discrete angular frequency in the Fourier domain. $N_{p,i}$ is defined as the length of the echo from the $i$th patch (in number of samples) captured by the range gate. It writes:

$$N_{p,i} = int \left( T_p \sum_{n=0}^{N-1} (p_r(t_n - t_{d,i}) G(t_n)) \right) \tag{2.8}$$

where $G(t)$ is a rectangular window representing the range gate, $p(t)$ is the transmit pulse envelope and $N$ is the number of samples in the integration period ($\frac{T_p}{T} + 1$). $f_{b,i}$ is the baseband frequency of the return from the $i$th patch, and takes into account the frequency shift due to the linear chirp and the Doppler frequency shift due to the relative spacecraft movement with respect to the Earth surface.

In this study, the parameterized SRF is compared to the SRF obtained analytically by means of eq. 2.6. The details about the implementation of eq. 2.6 are provided in section 3.
[4] show how to correct the land contaminated $\sigma_0$s by means of the LCR. The same methodology has been implemented in this study and is hereafter described. The basic hypothesis of this methodology is that the land and sea $\sigma_0$ contributing to the total measured $\sigma_0$ are uniform in the area of the target

wind vector cell. This is to say that the land and sea surfaces are spatially homogeneous over the integrated SRF of each WVC view. This hypothesis is rather acceptable in most of the areas away from human settlements. Furthermore, the contaminated $\sigma_0$ measurements should not exceed a threshold land contribution. Finally, it is supposed that the land contribution to $\sigma_0$ is proportional to the LCR. Under these hypothesis, the corrected $\sigma_0$ writes as follows:

$$\sigma_{0j}^C = \sigma_{0j} - \alpha LCR_j \; j \in 1, \ldots, M \tag{2.9}$$

Here $\sigma_{0j}$ represents the $j$-th measurement, $\sigma_{0j}^C$ its corrected value and $M$ is the total number of measurements with LCR values lower than a threshold value $\mathrm{LCR}^{th}$. $\alpha$ is the regression coefficient obtained by fitting all the $M$ measurements with a linear function:

$$\sigma_{0j} = \sigma_{0j}^C + \alpha LCR_j \; j \in 1, \ldots, M \tag{2.10}$$

Note that the accuracy of the sea backscatter of each view in a WVC is obtained by estimating the accuracy of the regression (equation 2.10) at $\alpha = 0$.

# 3 Methodology

$g_i$, the SeaWinds antenna gain pattern, is not published, and has not yet been made available by JPL. A theoretical antenna gain pattern that adequately models a dish antenna has been implemented. It writes

$$g_i = cos^4 \left( \sqrt{\left(\frac{d\phi_A}{2\theta_C}\right)^2 + \left(\frac{d\phi_E}{2\theta_C}\right)^2} \right) \tag{3.1}$$

with $\theta_C$ equal to $1^o$ and $d\phi_A$ and $d\phi_E$ representing respectively the azimuthal and elevation distances of the target point to the peak antenna gain axis. This formulation gives acceptable results, but it will be promptly changed in case the original SeaWinds antenna gain pattern will be made available by JPL.
$T_p$, the integration time, is set to 1.5 ms, while $T$, the sampling period, is set to the half of the inverse of the baseband width (BBW), in agreement with the sampling theorem. BBW has been set to 200 kHz.

Finally, $k_s$ and $k_e$ are set as follows:

$$k_s = k_c - n_k + 1 \tag{3.2}$$

$$k_e = k_c + n_k - 1 \tag{3.3}$$

$$k_c = nint\left(\frac{B_s}{2dk}\right) \tag{3.4}$$

$$dk = \frac{2BBW}{N-1} \tag{3.5}$$

with $B_s$ =7 kHz and $nint$ standing for nearest integer. In [1] $B_s$ is suggested to be set to 8.3 kHz, but this value seems to be excessive in our implementation. However, there are some parameters such as BBW and $T_p$ which are not explicitly set in [1], therefore, it is possible that a compensation occurs which justifies our different choice.
The accuracy of the LCR depends on the resolution of the LSM. The LSM used in this study derives from the Global Self-consistent Hierarchical High-resolution Geography (GSHHG) data base [7]. This database consists of a few global shoreline sets with different spatial resolutions. For this study, the highest available resolution has been used, which approximately corresponds to 100 m. The shoreline is used to pre-compute the LSM. In order to speed-up the computation of the LCR, the LSM is split in square tiles of 1000x1000 points, which are stored in LUTs indexed with latitude and longitude. Given the slice centroid position, only the pertinent tile and the eight adjacent ones are loaded in order to avoid any border effects. The LCR is then computed by dividing the weighted number of land points in the slice polygon by the total number of weighted points, cf. equation 2.1. Figure 2a shows an example of LSM tile in the region of the Eolian isles, in the southern Tyrrhenian sea, where land and sea points are depicted in red and black respectively. In order to have an idea of the spatial resolution of the LSM, a zoom over the Filicudi isle is shown in figure 2b (magenta frame of figure 2a).

In this study, $\mathrm{LCR}^{th}$ has been set to 0.5, but more sensitivity tests are needed in order to assess the most adequate value.

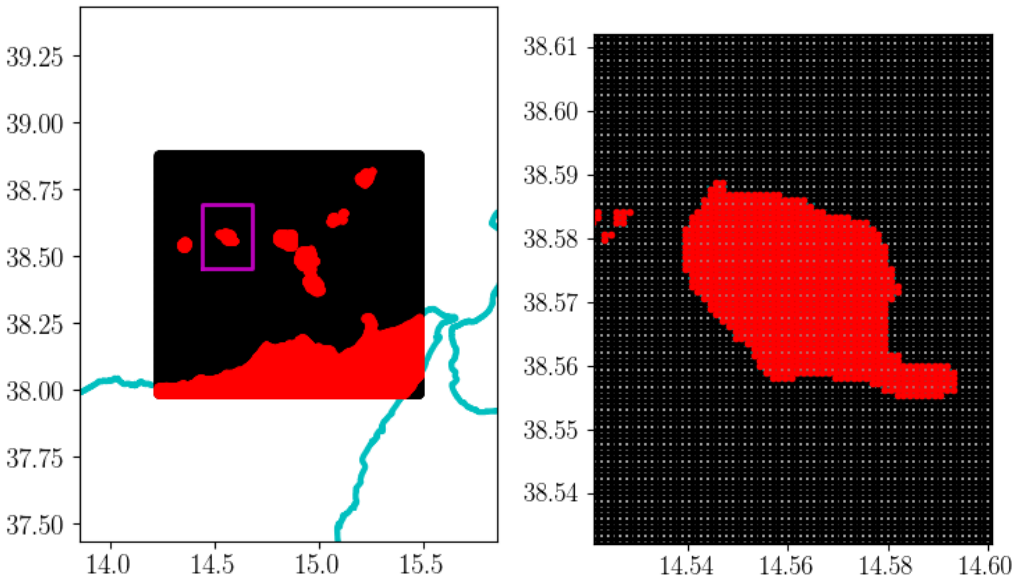


(a) LSM tile on the Eolian isles

(b) LSM on Filicudi

Figure 2

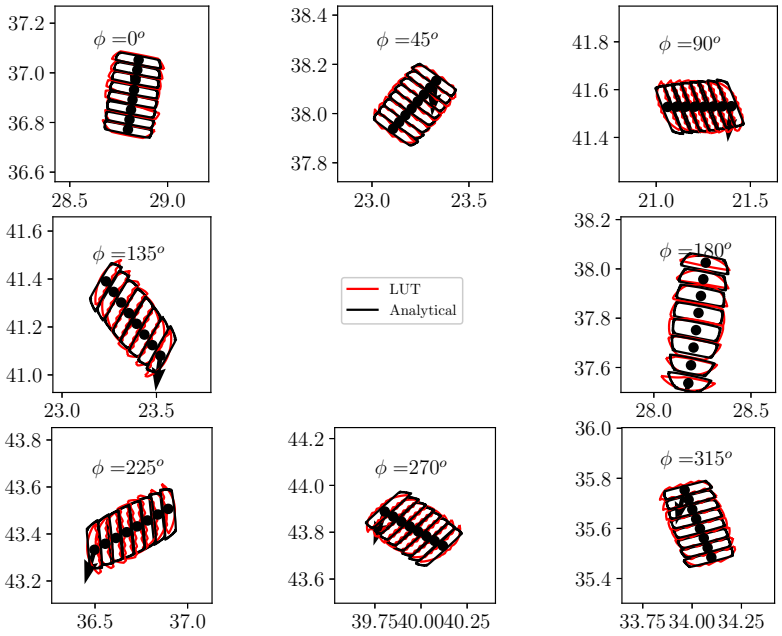


Figure 3: Black (red) lines: 3 dB analytical (LUT-derived) SRF contours computed for the inner beam with antenna azimuth angles varying from $0^o$ to $360^o$ with steps of $45^o$, for a descending orbit. Arrows indicate the spacecraft flying direction.

# 4 Results and discussion

The results shown in this section refer to the area test of the Gulf of Taranto, in the south of Italy.

Black lines of figure 3 (4) show the inner (outer) beam 3 dB SRF contours computed with the analytical method (eq. 2.6) while the red ones come from the LUT provided by Prof. Long. They are computed for the entire antenna azimuth range of values ($0^o$-$360^o$) with steps of $45^o$. The black arrows represent the spacecraft flying direction. Analytical and LUT derived contours are in good agreement, but some differences are apparent. LUT derived contours appear more jagged with respect to the analytical ones. In our opinion, this depends on the spatial resolution of the LUT. It is clear that this is nonphysical and, therefore, undesired.
Furthermore, analytical contours appear sometimes asymmetric with respect

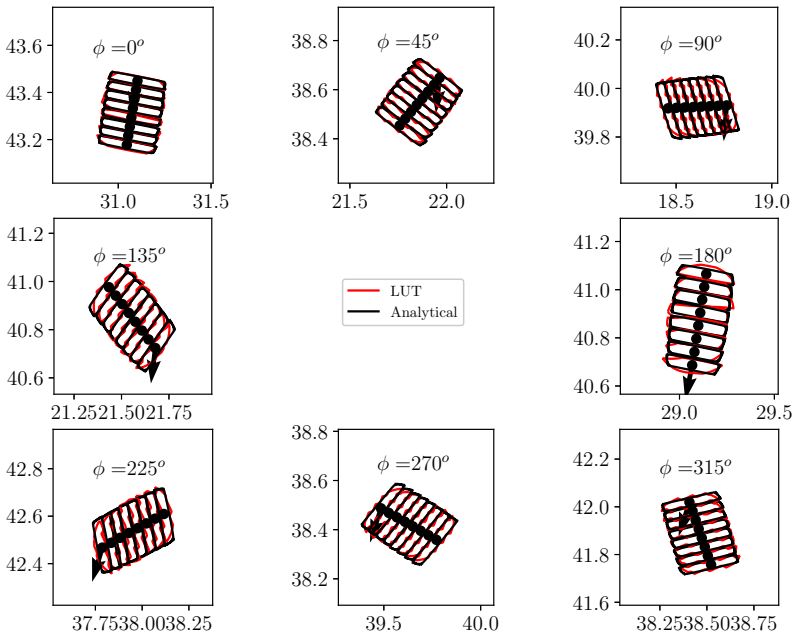


Figure 4: Black (red) lines: 3 dB analytical (LUT-derived) SRF contours computed for the outer beam with antenna azimuth angles varying from $0^o$ to $360^o$ with steps of $45^o$, for a descending orbit. Arrows indicate the spacecraft flying direction.

to the slice centroid, while those from LUT are not by construction, as stated in section 2. This feature is more apparent for mid-quadrant antenna azimuth angles ($45^0$, $135^o$, $225^o$ and $315^o$). Figure 5, which is a zoom of the northernmost slice depicted in figure 3, with antenna azimuth angle equal to $135^o$, may help to better understand this feature. Figure 5 shows the LUT derived 3 dB SRF contour in red, the analytical contour in black, the isolines of the antenna gain in magenta, the iso-range lines in cyan and the slice centroid with the black point. The range component of the SRF is similar to a box car, therefore the iso-range lines are all bunched together because of its steepness. The final visual effect is that of two unique thick lines. The region between the two thick cyan lines is characterized by the maximum value of the range component of the SRF, while the region outside has null values. Both the LUT derived and the analytical 3 dB contours lie between the two cyan lines, as expected. It is apparent that the range iso-lines are tilted with respect to the major ellipse axis of the iso-gain contours. Therefore, the final SRF cannot be symmetric with respect to the slice centroid.

Figure 6 shows the 3 dB SRF contours computed with the analytical method in black, and those derived from the LUT in red. The corresponding LCR values are indicated respectively in black and red. The LCR values are consistent with the shoreline and with each other. The maximum absolute difference between the two methods is 4% (second and fourth slice from up to down). The impact of these differences is expected to be significant, as currently a threshold of about 2% land contamination is used in the (non-coastal) processing, but the real impacts on the LCR-based $\sigma_0$ correction and the consequent wind field retrievals deserve further investigation.

In the remainder of this section, a set of $\sigma_0$ measurements relating to a coastal wind vector cell (WVC) will be shown. The test case analysed here refers to the coastal area off-shore the city of Nardò, in the south of Italy. Figure 7 shows the test case area, with the red pin stating the position of the WVC grid point.

Figure 8a (8b) shows the 3 dB SRF contours of all the selected measurements (those with LCR<0.5) around the WVC grid point. The magenta point represents the WVC grid point, while the orange one stands for the slices ensemble centroid. All the depicted contours are computed with the analytical method. Measurements are selected according to the following criteria: 1) the slice centroid is within 15 km from the WVC centre; 2) each measurement is quality controlled (QCed) according to the indications provided in the QuikSCAT user's manual [8]. For each slice $\sigma_0$ the following conditions are required: a) the antenna gain is acceptable (higher than a given threshold value); b) $\sigma_0 > 0$; c) SNR is acceptable (higher than a given threshold value); d) the slice center is located. When the condition

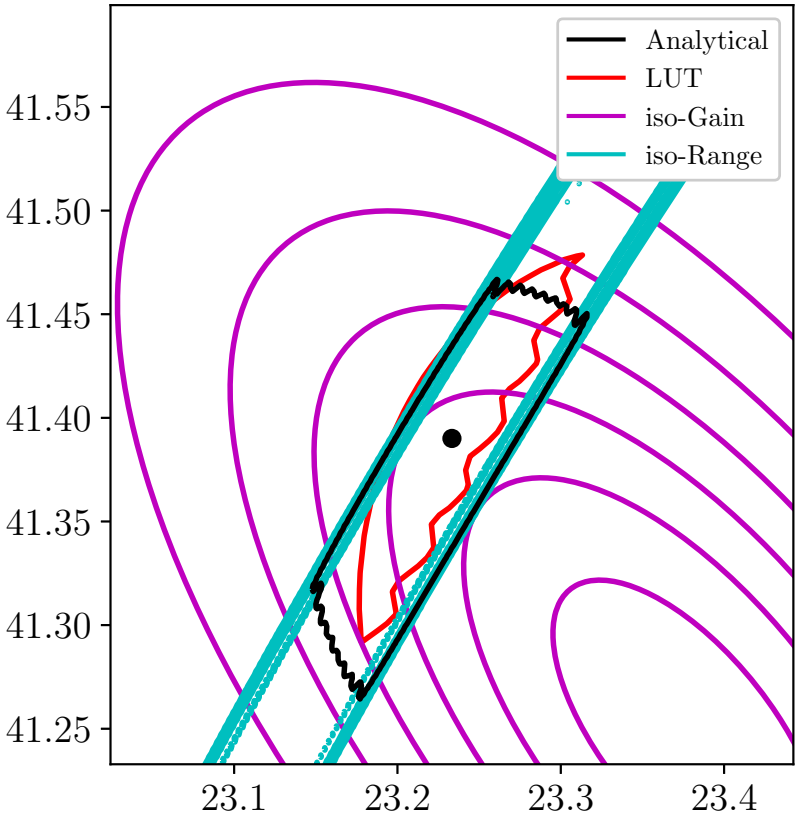


Figure 5: Magenta lines: isolines of the antenna gain pattern. Cyan lines: iso-range lines. Black (red) line: 3 dB SRF Analytical (LUT-derived) contour. Black point: slice centroid.

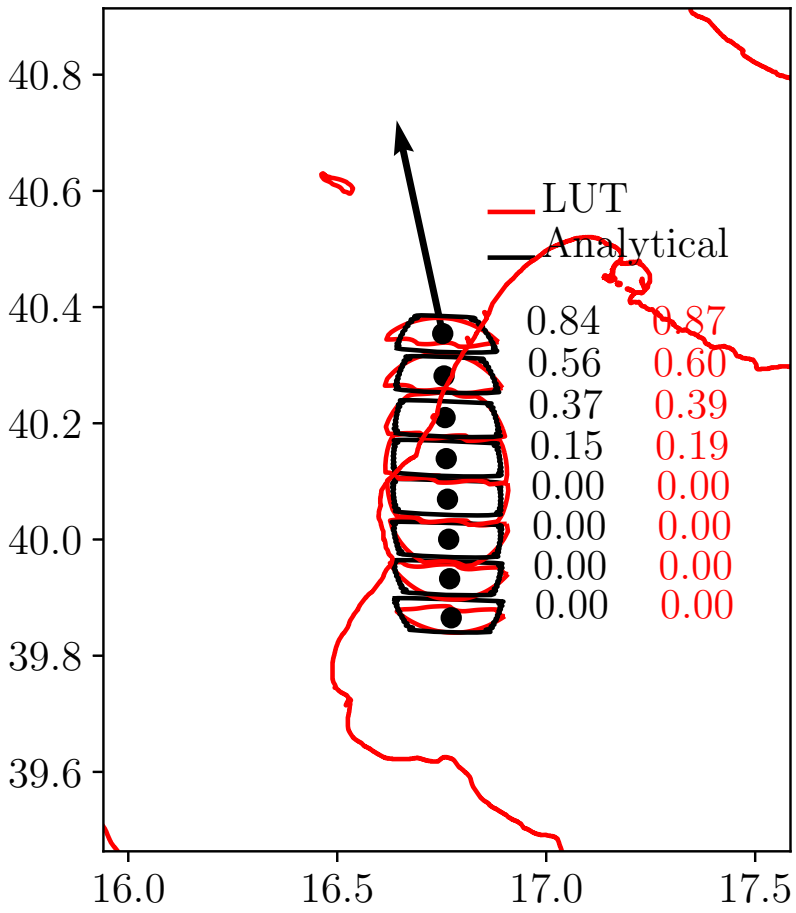


Figure 6: Black (red) lines: 3 dB analytical (LUT-derived) SRF contours. Black (red) text: LCR values relating to the analytical (LUT-derived) contours. Black points: slice centroids. Black arrow: spacecraft flying direction.


Figure 7: Map of the test case area. The red pin represents the WVC grid point of the test case.

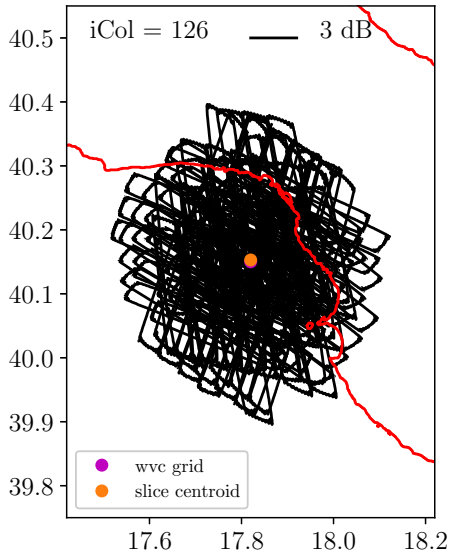


(a) 3 dB SRF contours before LCR filtering. Magenta (orange) point: WVC grid point (slices ensemble centroid)

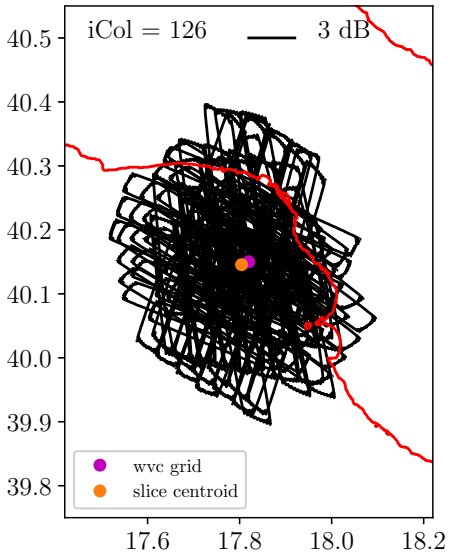


(b) 3 dB SRF contours after LCR filtering. Magenta (orange) point: WVC grid point (slices ensemble centroid)

Figure 8

is respected the corresponding flag value is equal to 0 (absence of condition), otherwise it is equal to 1 (presence of condition). Furthermore, it is required that the Data Quality Flag, the Sigma0 Usability Flag and the flag $frame\_err\_status$ are all equal to 0. If Data Quality Flag is equal to 0, it means that most (it not all) of the data in the corresponding telemetry are valid, otherwise they are suspect; if Sigma0 Usability Flag is equal to 0, then the data which pertain to the corresponding whole scatterometer pulse are valid; finally $frame\_err\_status = 1$ indicate potential problems due to instrument error or poor communication with the spacecraft. The QC is applied in the most conservative way, requiring the absence of any conditions. The total number of measurements is 127, 117 of which pass the QC and 10 are rejected.

This test case refers to a WVC grid point in the so called "sweet zone" of the scatterometer swath, for which the configuration of the four scatterometer views (fore horizontal (HHF), fore vertical (VVF), aft horizontal (HHA) and aft vertical (VVA), i.e., WVC numbers between 18 (88) and 56 (136) on the left (right) side of the swath) is optimal for wind retrieval purposes (i.e., good azimuth diversity). Figure 9 shows the distribution of the antenna azimuth angles for the entire set of measurements.

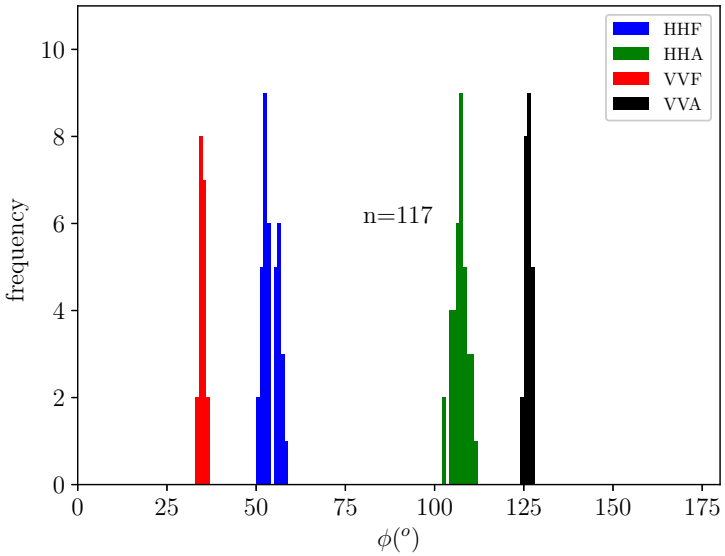


Figure 9: Distribution of the antenna azimuth angles for all the measurements. HH (VV) stands for horizontally (vertically) polarized pulse and F (A) stands for fore (aft).

Figure 11 shows the scatter plot of the LCR values versus the $\sigma_0$s. The points of the plot are coloured according to the scatterometer views. A couple of things are apparent. First, the range of values of $\sigma_0$ is rather wide, in particular for LCR=0, suggesting that they are very noisy (low wind) or not properly QCed. In particular, the range of values without any land contribution (LCR=0) is excessively wide. Two values of $\sigma_0$ are almost -10 dB, which is very high, considering that the local wind speed is lower than 4 $ms^{-1}$ (from level 2 QuikSCAT files), but which may be outer slices with poor radar illumination. Of further concern are the many low backscatter values, which do not appear for LCR>0 in this region and are well below the visual linear regression point (although the plot is in dB and not in linear units). Figure 12 shows the distribution of the simulated $\sigma_0$s by means of the Geophysical Model Function (GMF) NSCAT4 in blue and the distribution of the measured $\sigma_0$s in orange for each subplot. Furthermore, the red line shows the distribution of the simulated $\sigma_0$s for each scatterometer view (HHF, HHA, VVF, VVA) while the cyan line shows the distribution of the measured $\sigma_0$s. The differences between the measured and the simulated $\sigma_0$s are certainly attributable to problems affecting the measurements. This aspect deserves further investigation.

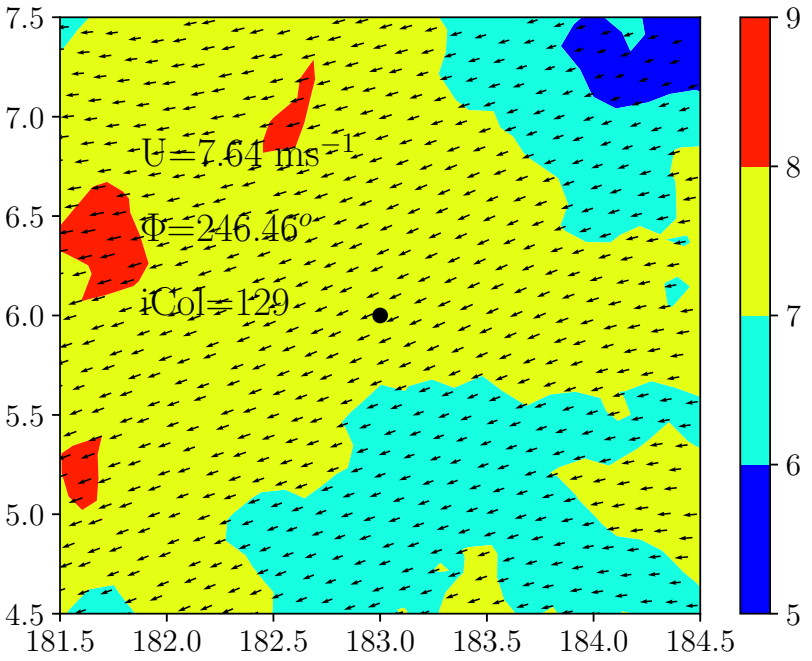


Figure 10: Map of the wind field for the open ocean test case (from QuikSCAT L2B products). The WVC grid point is depicted in black.

Figure 13 shows the simulated and the measured $\sigma_0$s for a WVC grid point situated in open ocean, where the trade winds blow. As shown in figure 10, in this case, the wind field is rather stable, characterized by a uniform wind direction of approximately $246^o$ and a wind speed of approximately 7.5 ms$^{-1}$.

In this case, the distribution of the measured $\sigma_0$s is narrower with respect to the previous case. Once more, the aspect relating to the $\sigma_0$ noise characterization deserves more investigation.
Second, the trend with LCR is approximately linear if one considers only the values of LCR greater than 0.

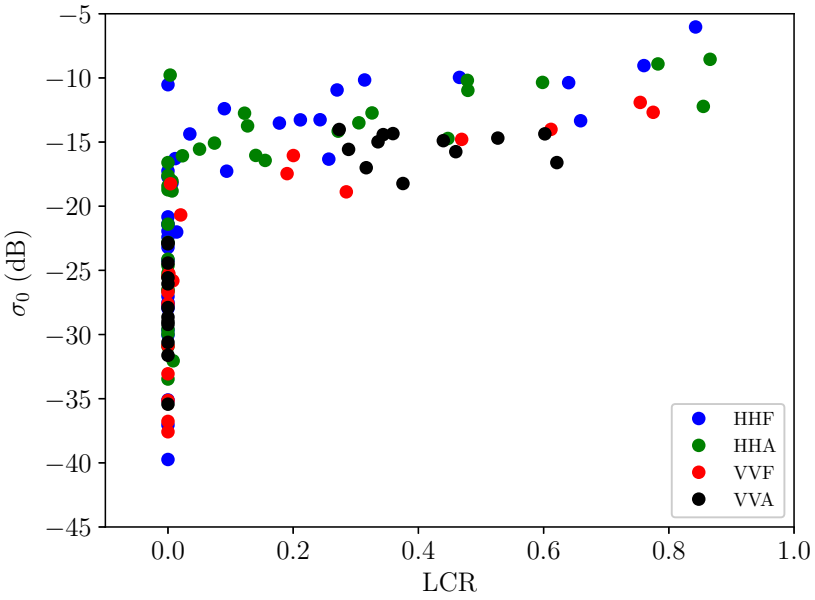


Figure 11: Scatter plot of LCR values vs $\sigma_0$s. HH (VV) stands for horizontally (vertically) polarized pulse and F (A) stands for fore (aft).

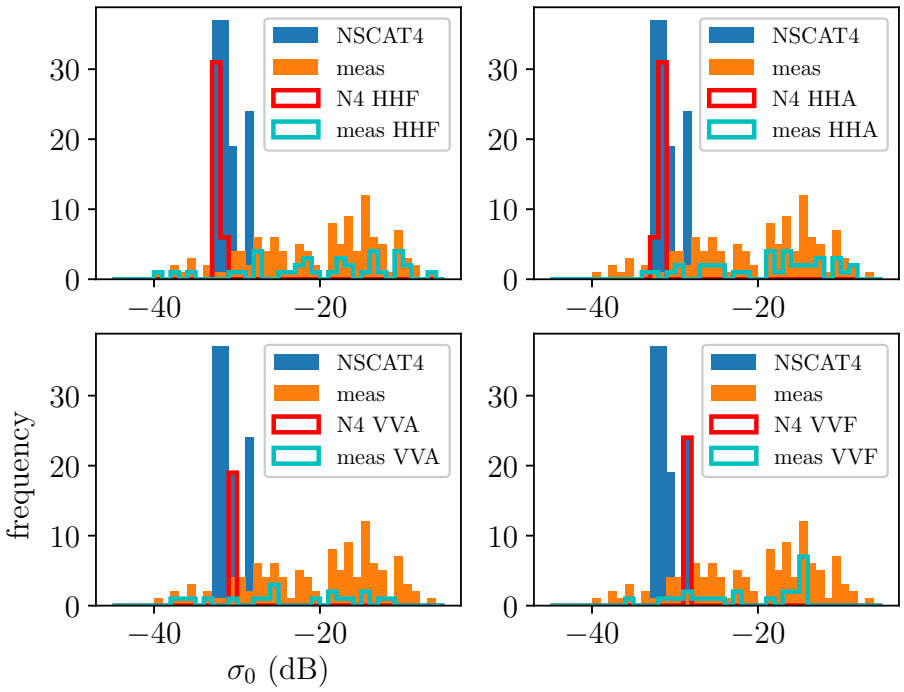


Figure 12: Common patterns to all subplots: the distribution of the simulated (measured) $\sigma_0$s with the GMF NSCAT4 for the test case (red pin of figure 7) is depicted in blue (orange). In the top left (top right, bottom left, bottom right) corner subplot, red (cyan) line represents the distribution of the simulated (measured) $\sigma_0$s for the view HHF (HHA, VVF, VVA). HH (VV) stands for horizontally (vertically) polarized and A (F) stands for aft (fore).

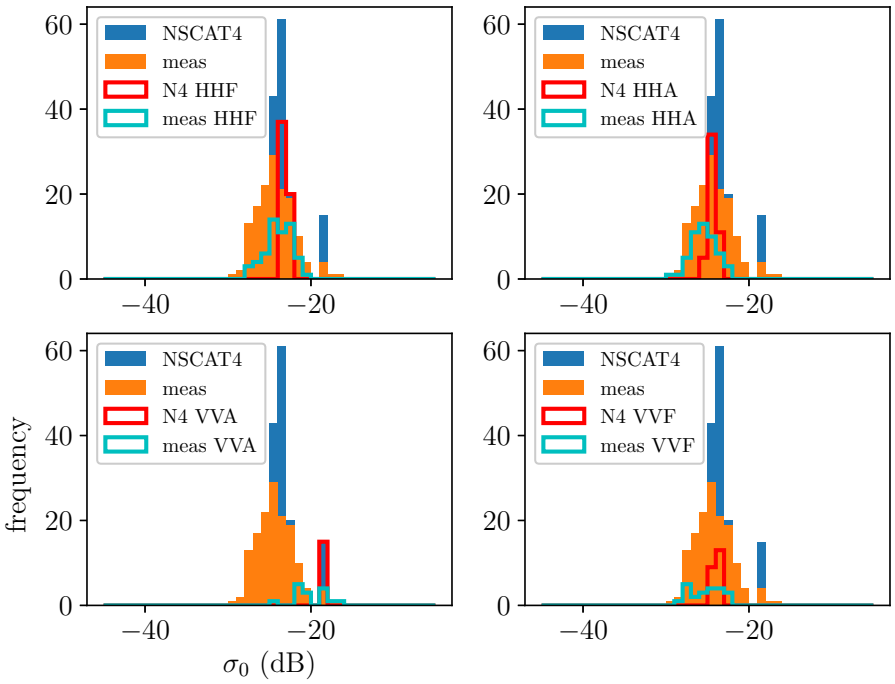


Figure 13: Common patterns to all subplots: the distribution of the simulated (measured) $\sigma_0$s with the GMF NSCAT4 for the open ocean test case is depicted in blue (orange). In the top left (top right, bottom left, bottom right) corner subplot, red (cyan) line represents the distribution of the simulated (measured) $\sigma_0$s for the view HHF (HHA, VVF, VVA). HH (VV) stands for horizontally (vertically) polarized and A (F) stands for aft (fore).

# 5 Conclusions

The SeaWinds Spatial Response Function (SRF) has been analytically modeled according to [6], and it has been visually validated by comparing it with that derived from the look-up-table (LUT) provided by Prof. Dave Long of the Brigham Young University. The LUT may be queried with the following input: the antenna azimuth angle, the orbit time, the beam identifier, the egg centroid latitude, and the node index. Then, the SRF is centered around the slice centroid. The two SRF models are in good agreement, even if some differences are apparent. In particular, the LUT derived SRFs are generally more jagged with respect to those from the analytical model. Furthermore, analytical SRFs may be asymmetric with respect to the slice centroid, while those derived from the LUT are not because of the re-positioning step. It has been demonstrated that these asymmetries are physical, therefore expected. The derived Land Contribution Ratios (LCRs) are compared with each other, showing a general agreement and visual consistency with the shoreline. The assessment of the impact of their differences (up to 3%) on the wind field retrievals deserves further investigation. A coastal test case in the Gulf of Taranto (south of Italy) has been analyzed. Two main aspects are revealed in this analysis: a) the distribution of the slice $\sigma_0$ values is excessively wide and many values are much higher than expected; b) the $\sigma_0$ has a linear trend with respect to the LCR, when land contamination is present (LCR>0). For what concerns point a), it emerges that the thorough characterization of the slice $\sigma_0$ noise and its exploitation in the sea backscatter value regression (equation 2.10) is fundamental for a successful retrieval of the wind field. This aspect deserves a dedicated study. A procedure for the correction of the land contaminated $\sigma_0$ values has been implemented following [4] even if it has not yet been tested. This is also left for a future study.

# 6 Future work

One of the main outcomes of this study is that full resolution (FR) QuikSCAT $\sigma_0$s are noisy or not properly indexed or QCed. It is strongly recommended to thoroughly and further characterize the slice $\sigma_0$ noise in coastal and open ocean areas. This is essential for a successful QC and needed for applying weights in the regression for correction of the land-contaminated measurements. In particular, it is expected that peripheral slices with respect to the egg centroid are noisier than central slices due to the limited effective area illuminated (low value of $S_i$ in equation 2.6) and a weighting procedure may therefore be beneficial. This information is also relevant for the retrieval stage, where a weighted averaging procedure of the QCed and corrected measurements could be preferred over the current boxcar averaging. The measurement noise characterization should be first performed in open ocean test areas of well-known stable wind conditions (such as those of trade winds) and for different wind regimes. Then, specific coastal test areas which are not affected by either orography or human presence, e.g., delta areas, atolls in the Pacific, will be considered for verification of the LCR-based backscatter correction, QC, and averaging. The coastal processor should be set up according to the flow chart described in figure 14.

In particular, the processor needs two different inputs: a) FR measurements; b) the WVC grid for retrieval purposes. The former is provided by the QuikSCAT level 1B (L1B) FR data files while the latter can be obtained from the QuikSCAT level 2a (L2A) files by means of the KNMI "hdf2bufr" tool. The WVC grid and FR information can be used to first compute the SRF, then the LCR and finally the corrected $\sigma_0$. The QuikSCAT antenna gain patterns will be embedded in the processor. At the moment, this information is not publicly available and will hopefully be provided by the NASA JPL team responsible for QuikSCAT data products. Alternatively, the analytical model already implemented in this study will be used, which appears to perform well. Once the coastal processor is ready, the wind field retrievals can be validated with winds from moored buoys and models. It is also recommended investigte the sensitivity of the retrievals with respect to the SRF computation methodology (analytical or from LUT), the radius around the WVC grid point, the LCR-based $\sigma_0$ correction algorithm, the LCR threshold value and the distance to the coast. Most of these recommendations have been resumed in the new Visiting Scientist Activity (VSA) follow-on proposal [9], which has been recently accepted by EUMETSAT.

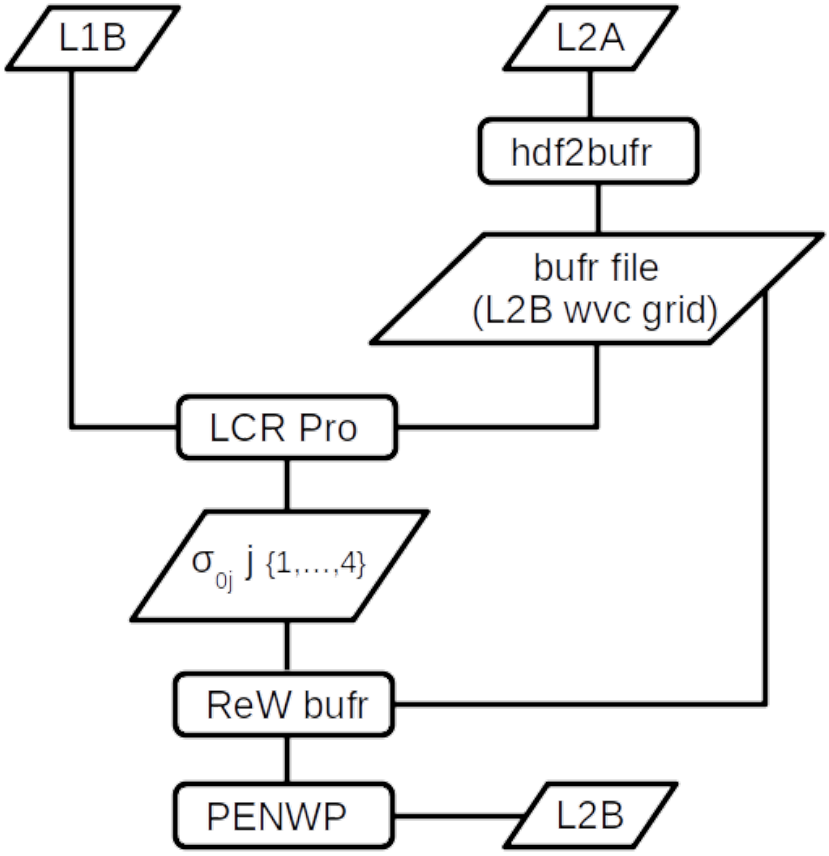


Figure 14: Flow chart of the coastal processor.

## Acknowledgements

The authors of this report would like to acknowledge Prof. Dave Long from the Brigham Young University for providing the Look-Up Table of pre-computed QuikSCAT Spatial Response Functions and for the precious support during the entire course of the project. Furthermore they would like also to acknowledge Dr. Bryan Stiles and Dr. Roy Scott Dumbar from the NASA Jet Propulsory Laboratory for their support with QuikSCAT files.

# References


[1] M. P. Owen and D. G. Long, "Land-contamination compensation for quikscat near-coastal wind retrieval," *IEEE Transactions on Geoscience and Remote Sensing*, vol. 47, no. 3, pp. 839–850, 2009.

[2] R. D. Lindsley, C. Anderson, J. Figa-Saldaña, and D. G. Long, "A parameterized ascat measurement spatial response function," *IEEE Transactions on Geoscience and Remote Sensing*, vol. 54, no. 8, pp. 4570–4579, 2016.

[3] R. D. Lindsley, J. R. Blodgett, and D. G. Long, "Analysis and validation of high-resolution wind from ascat," *IEEE Transactions on Geoscience and Remote Sensing*, vol. 54, no. 10, pp. 5699–5711, 2016.

[4] J. Vogelzang and A. Stoffelen, "Ascat land correction, report for the eumetsat ocean and sea ice saf," tech. rep., Koninklijk Nederlands Meteorologisch Instituut, 2020. SAF/OSI/CDOP3/KNMI/TEC/TN/384.

[5] "https://nwp-saf.eumetsat.int/site/software/scatterometer/."

[6] M. W. Spencer, C. Wu, and D. G. Long, "Improved resolution backscatter measurements with the seawinds pencil-beam scatterometer," *IEEE Transactions on Geoscience and Remote Sensing*, vol. 38, no. 1, pp. 89–104, 2000.

[7] P. Wessel and W. H. F. Smith, "A global, self-consistent, hierarchical, high-resolution shoreline database," *Journal of Geophysical Research: Solid Earth*, vol. 101, no. B4, pp. 8741–8743, 1996.

[8] Thorlabs, *QuikSCAT Science Data Product. User's Manual*. JPL NASA.

[9] A. Stoffelen, "The use of full resolution quikscat backscatter noise for coastal wind retrieval." EUMETSAT Visiting Scientist Activity proposal, 2020.